Electronic Supplementary Material (ESI) for Journal of Materials Chemistry A.
This journal is © The Royal Society of Chemistry 2024

Supplementary Information for

Drag Reduction and Antifouling of Spontaneous Fast Moving Air Film

Defeng Yan[1, 2], Junyi Lin[1], Bingzhen Zhang [1], Song Zhang[1], Siying Ling[3*], and Jinlong Song[1, 2*]

1 State Key Laboratory of High-performance Precision Manufacturing, Dalian University of Technology, Dalian Liaoning, 116024, China.

2 Key Laboratory for Micro/Nano Technology and System of Liaoning Province, Dalian University of Technology, Dalian Liaoning, 116024, China.

3 College of Engineering, Shantou University, Shantou Guangdong, 515063, China

*Corresponding author: songjinlong@dlut.edu.cn; syling@stu.edu.cn

Content

Figures

Tables

Videos

Figures

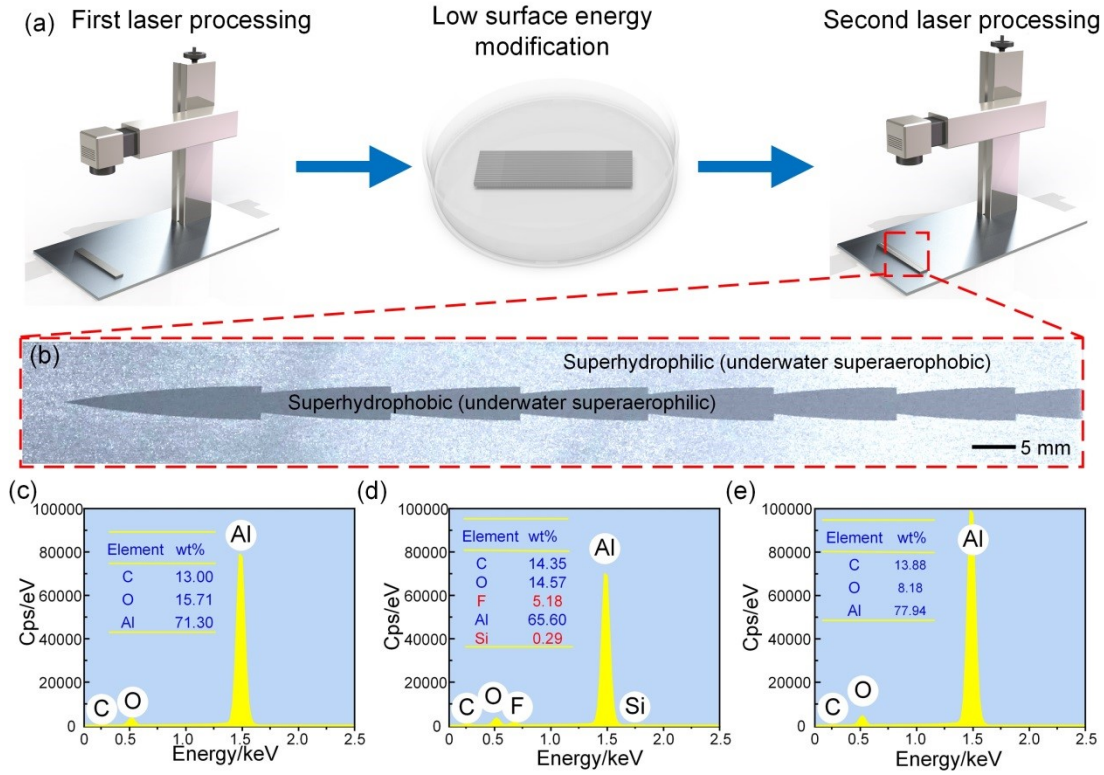

Figure S1. Schematics of the fabrication processes of the serial brachistochrone-shaped pattern (SBP) and sample characterization. (a) Schematics of the fabrication processes of the SBP, where the laser parameter are the laser power of 15 W, line spacing of 50 μm, and scanning velocity of 500 mm/s. (b) Image of the SBP. (c) Superhydrophilic Al surface after the first laser etching. (d) Superhydrophobic surface after FAS modification. After modification with the FAS, F and Si element appeared. (e) Superhydrophilic region after the second laser etching. F and Si elements were not detected on the superhydrophilic region after laser etching, indicating that the FAS layer was removed.

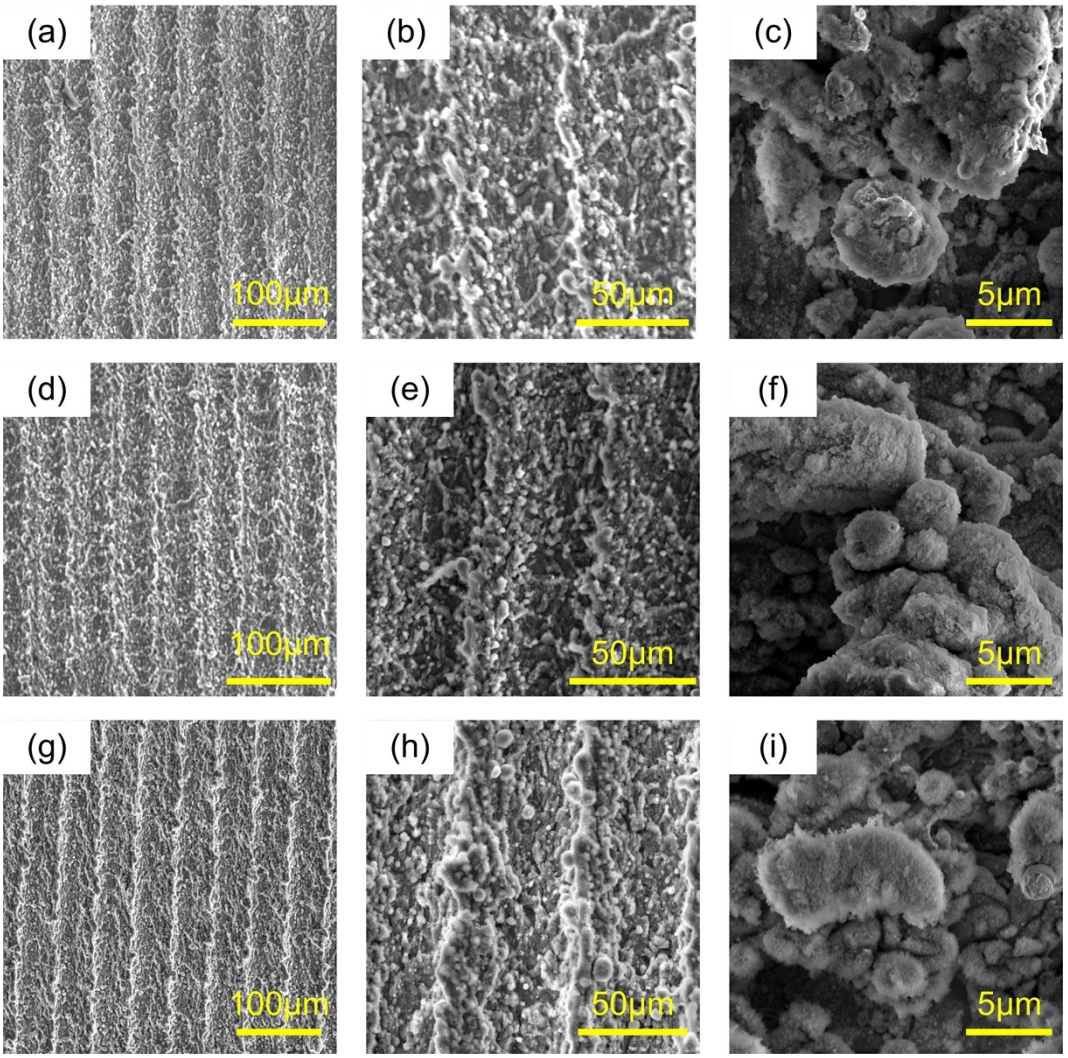

Figure S2. SEM images of the Al surface after the first laser process, the Al surface after the low surface energy modification, and the Al surface after the second laser process. The SEM images of Al surface at the 500 times magnification (a), 1500 times magnification (b), and 10000 times magnification (c) after the first laser process. The SEM images of Al surface at the 500 times magnification (d), 1500 times magnification (e), and 10000 times magnification (f) after the low surface energy modification, which is superhydrophobic region of the SBP. The SEM images of Al surface at the 500 times magnification (g), 1500 times magnification (h), and 10000 times magnification (i) after the second laser process, which is superhydrophilic region of the SBP.

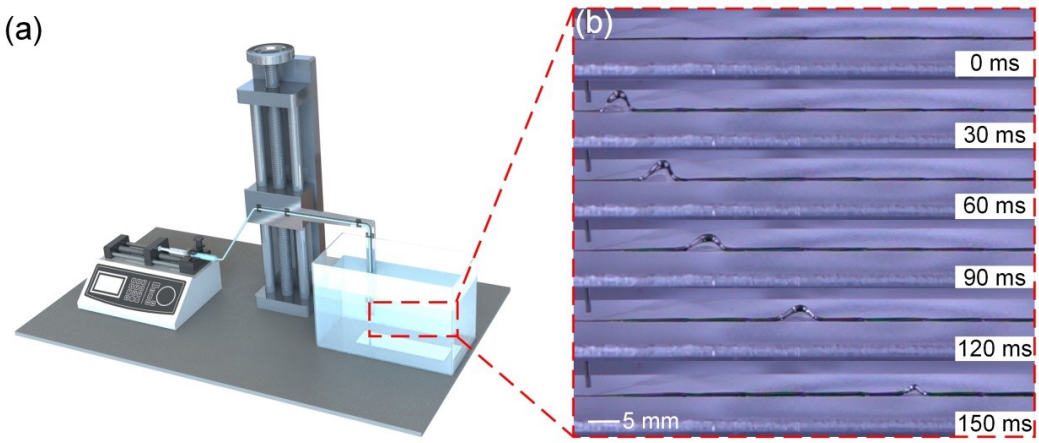

Figure S3. Schematics of the underwater air bubble transportation experiment system and transportation processes of a 40 μL air bubble on the SBP. (a) Schematics of the underwater air bubble transportation experiment system. (b) Transportation processes of a 40 μL air bubble on the SBP. In this work, we calculated the average air bubble transportation velocity of a 40 μL air bubble with an 80 mm transportation distance to evaluate whether our designed SBP was superior.

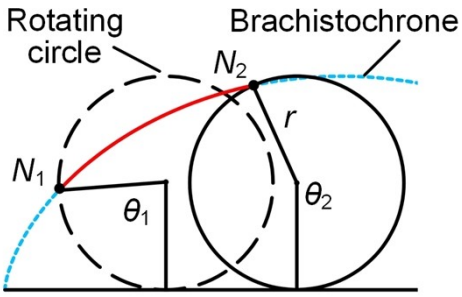

Figure S4. Schematics of the brachistochrone curve, where r, θ_1, and θ_2 were the rotating circle radius, angle which the rotating circle rotated from its origin position to the starting position of single pattern, and angle which the rotating circle rotated from its origin position to the ending position of single pattern, respectively.

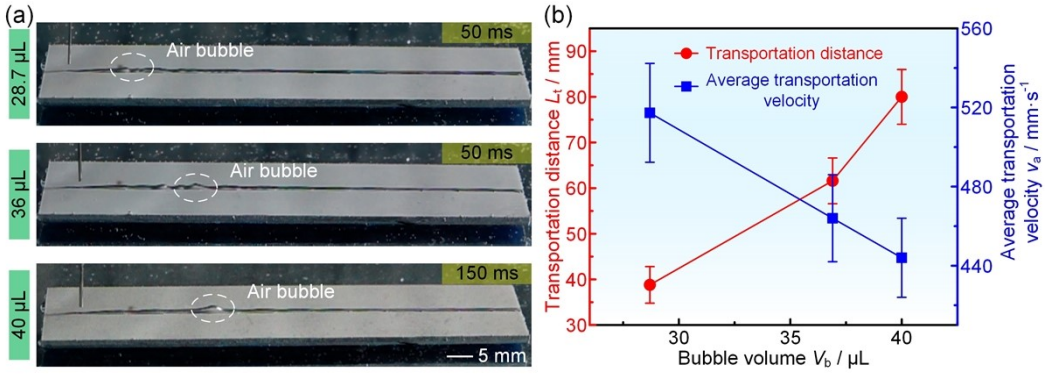

Figure S5. The air bubble with different volumes can transport on the SBP. (a) Images of the air bubble with different volumes transported on the SBP. (b) The variation of the transportation distance with different bubble volumes and the variation of the average transportation velocity with different bubble volumes.

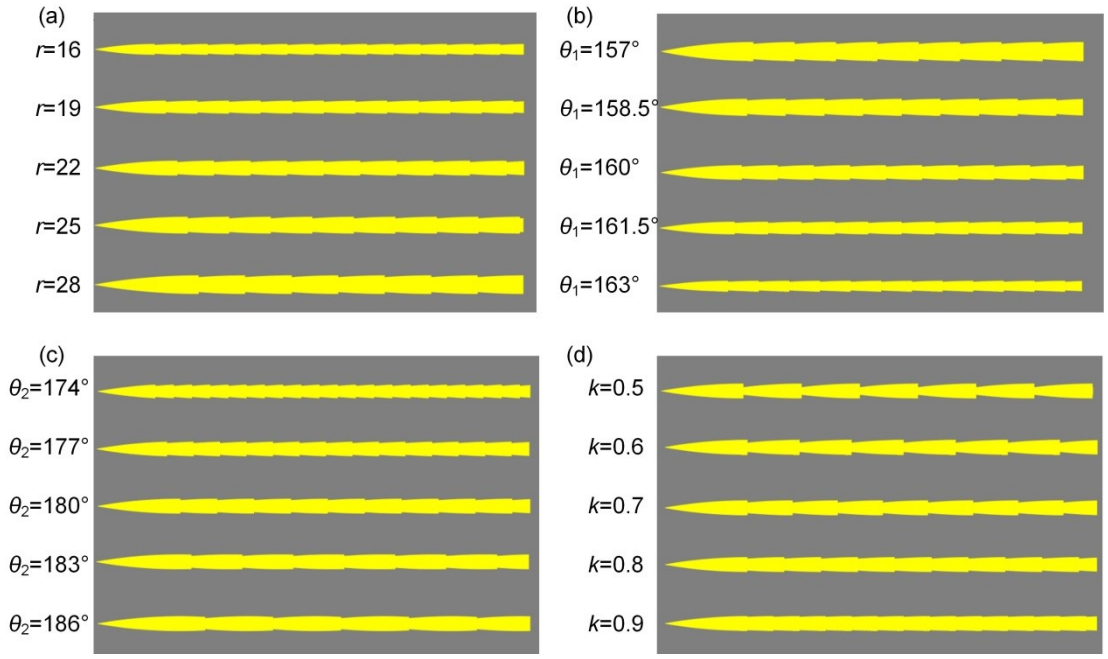

Figure S6. Schematic of the SBP with the different parameters. (a) Schematic of the SBP with the start rotation angle of 160°, the end rotation angle of 180°, and the ratio of narrow width to wide width of 0.8 at the different rotating circle radii. (b) Schematic of the SBP with the rotating circle radius of 22 mm, the end rotation angle of 180°, and the ratio of narrow width to wide width of 0.8 at the different start rotation angles. (c) Schematic of the SBP with the rotating circle radius of 22 mm, the start rotation angle of 160°, and the ratio of narrow width to wide width of 0.8 at the different end rotation angles. (d) Schematic of the SBP with the rotating circle radius of 22 mm, the start rotation angle of 160°, and the end rotation angle of 180° at the different ratios of narrow width to wide width.

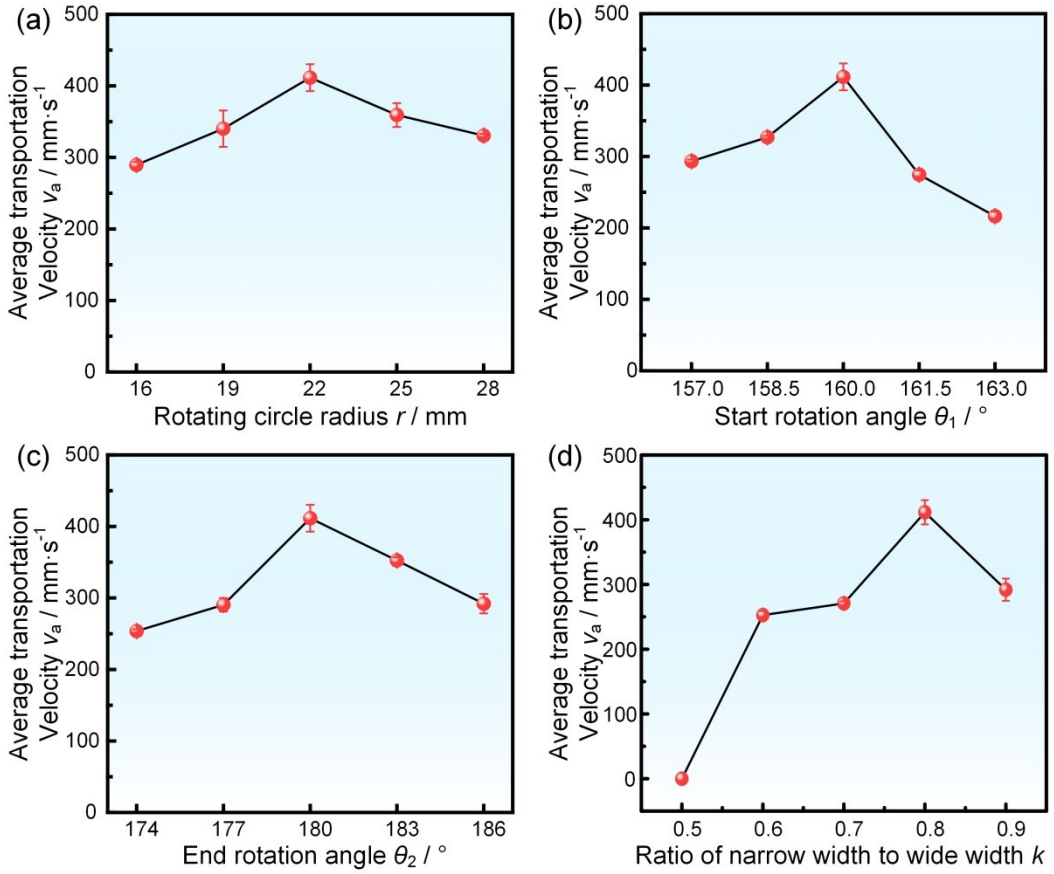

Figure S7. The average bubble transportation velocity on the SBP with the different parameters. (a) The variation of the average transportation velocity with the increasing of the rotating circle radius. (b) The variation of the average transportation velocity with the increasing of the start rotation angle. (c) The variation of the average transportation velocity with the increasing of the end rotation angle. (d) The variation of the average transportation velocity with the increasing of the ratio of narrow width to wide width.

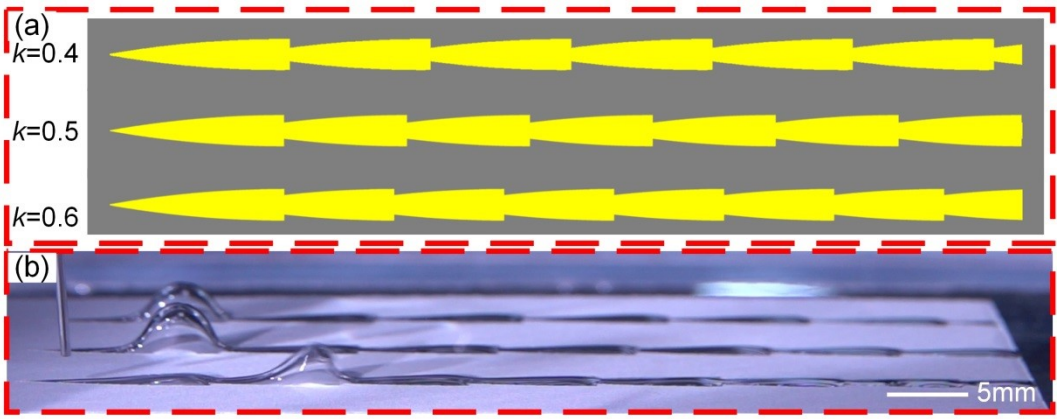

Figure S8. Schematic of the SBP with the different ratios of narrow width to wide width (k) and images of the air bubble on the SBP. (a) Schematic of the SBP with k=0.4 & 0.5 & 0.6. (b) Images of the 40 μL air bubble on the SBP with k=0.4 & 0.5 & 0.6.

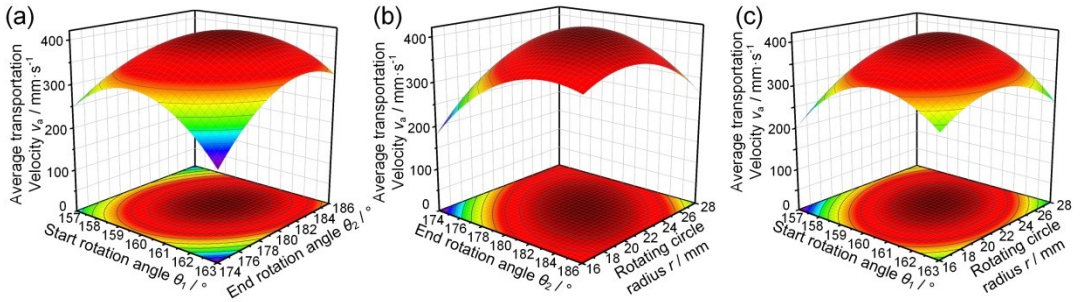

Figure S9. The responsive surface for the interaction influence between the SBP parameters. (a) The responsive surface for the interaction influence between the start rotation angle and the end rotation angle on the average transportation velocity. (b) The responsive surface for the interaction influence between the end rotation angle and the rotating circle radius on the average transportation velocity. (c) The responsive surface for the interaction influence between the start rotation angle and the rotating circle radius on the average transportation velocity.

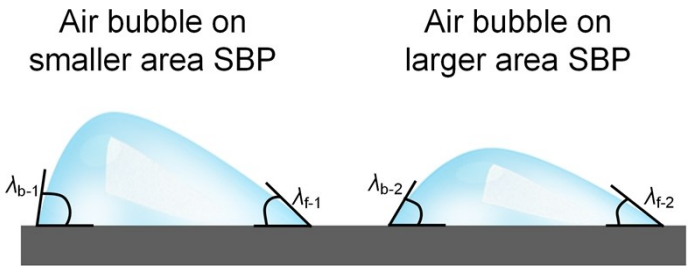

Figure S10. Schematic of the air bubble on the SBP with different areas. The larger SBP area results in that the air bubble were more spread out on the SBP, which means the difference of air contact angle between the front and the backside of the air bubble became smaller.

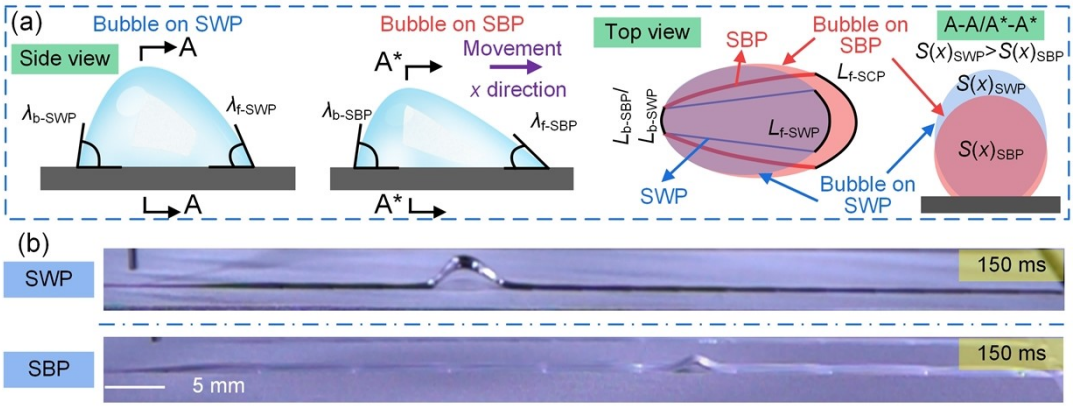

Figure S11. Force analysis of the bubble on the serial wedge-shaped pattern (SWP) and SBP (a) and images of the air bubble on the SWP and the SBP (b). As shown in Figure S9(a), when the bubble was located at the same position of the SBP and the SWP, the λ_b of the SBP ($\lambda_{b\text{-}SBP}$) and the l_b of the SBP ($l_{b\text{-}SBP}$) were same as the λ_b of the SWP ($\lambda_{b\text{-}SWP}$) and the l_b of the SWP ($l_{b\text{-}SWP}$). However, due to the variable curvature curve of the SBP, the l_f of the SBP ($l_{f\text{-}SBP}$) was wider than the l_f of the SWP ($l_{f\text{-}SWP}$), which made that the air bubble more easily spread on the SBP, resulting in that the λ_f of the SBP ($\lambda_{f\text{-}SBP}$) being less than the λ_f of the SWP ($\lambda_{f\text{-}SWP}$). Based on the aforementioned analysis and Equation S1,

$$F_L \sim \gamma l_f \cos\lambda_f - \gamma l_b \cos\lambda_b \tag{S1}$$

it could be found that the Laplace force of the bubble on the SBP was larger than that on the SWP. In addition, since the air bubble more easily spread on the SBP than that on the SWP, the $S(x)$ of the SBP ($S(x)_{SBP}$) was less than the $S(x)$ of the SWP ($S(x)_{SWP}$), which meant that the F_W of the SBP ($F_{W\text{-}SBP}$) was less than the F_W of the SWP ($F_{W\text{-}SWP}$). According to the Equation S2,

$$F = F_L + F_C - F_W - F_P \tag{S2}$$

the bubble had the greater driving force from the Laplace pressure and the smaller resistance force from the water on the SBP compared with that on the SWP, which was why the bubble transported faster on the SBP than that on the SWP (Figure S9(b)).

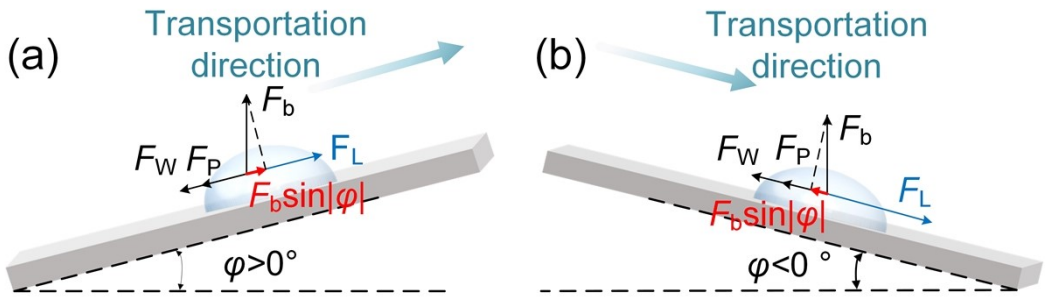

Figure S12. Free body diagrams of the bubble on the inclined surface. (a) Schematics of the bubble on the inclined surface with the inclination angle larger than 0. (b) Schematics of the bubble on the inclined surface with the inclination angle less than 0.

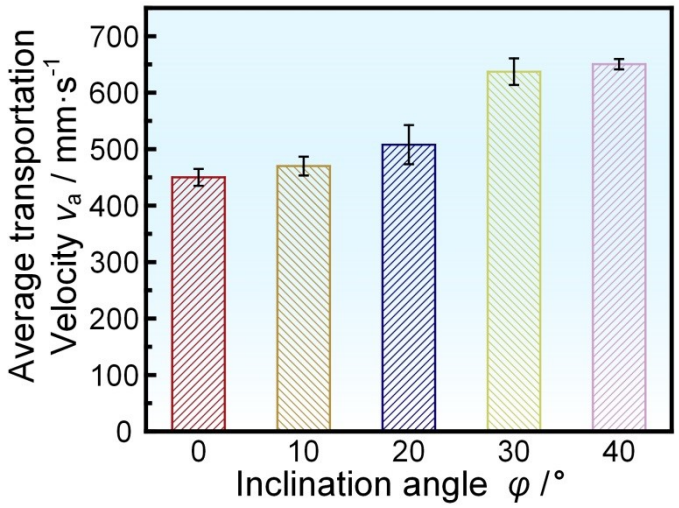

Figure S13. The variation of the average transportation velocity with the increasing of the inclination angle.

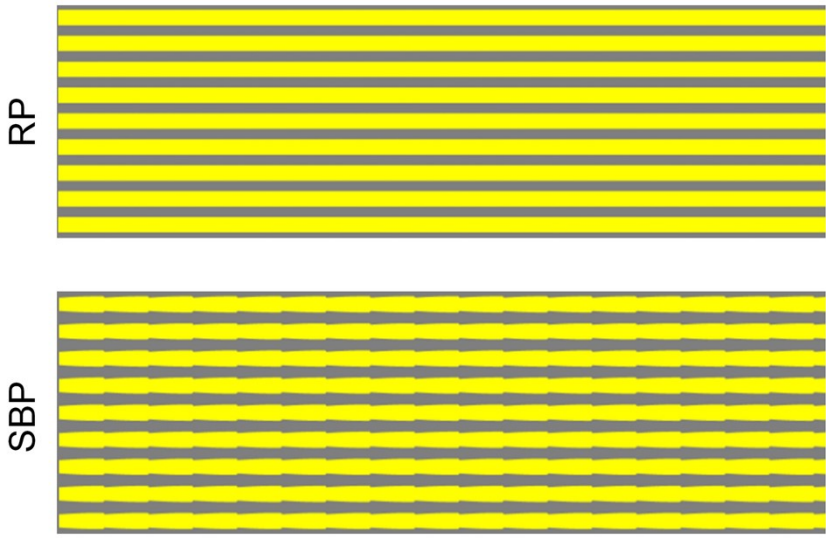

Figure S14. Schematic of the samples of 9 RP or 9 SBP for the underwater drag reduction.

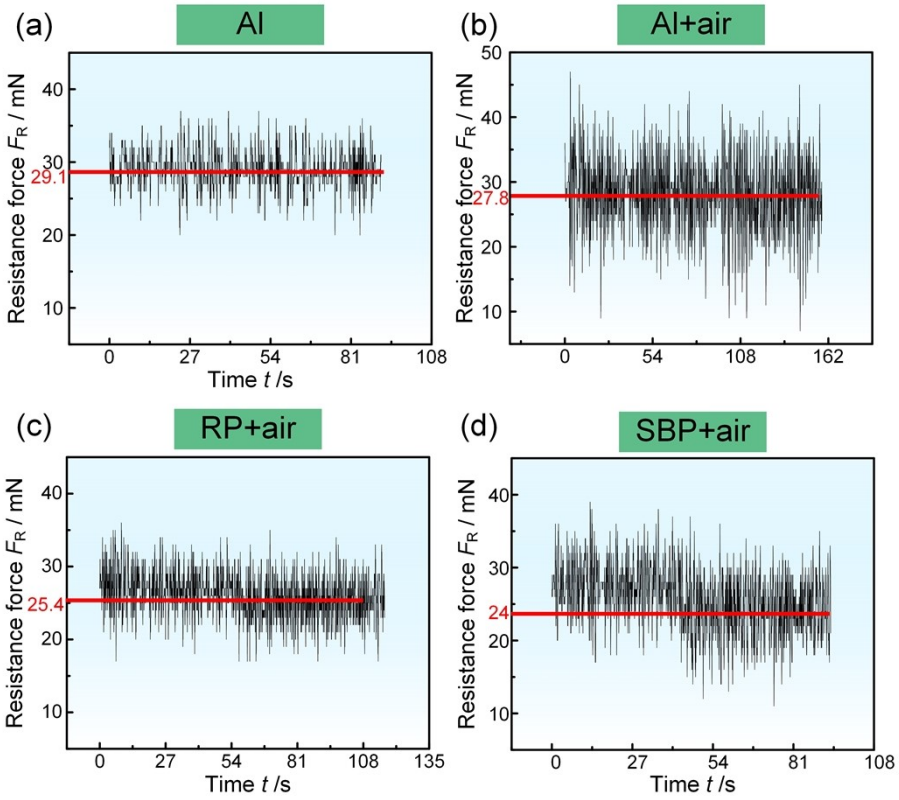

Figure S15. The underwater resistance force of the common Al surface, common Al surface with bubble supply, RP with bubble supply, and SBP with bubble supply. (a) The underwater resistance force of the common Al surface. (b) The underwater resistance force of the common Al surface with bubble supply. (c) The underwater resistance force of the RP with bubble supply. (d) The underwater resistance force of the SBP with bubble supply. The underwater drag reduction rates of the common Al surface with bubble supply, RP with bubble supply, and SBP with bubble supply are 4.5%, 12.7%, 17.5%, respectively.

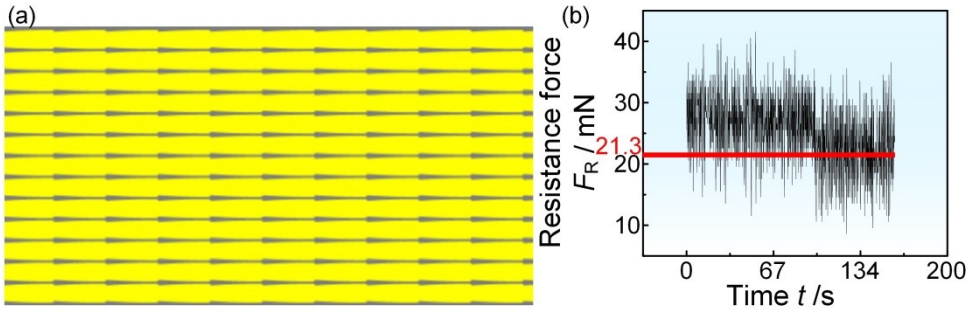

Figure S16. Schematic of the sample with 13 SBP (a) and the underwater resistance force of the sample with 13 SBP (b). For the sample with 40 mm width and 200 mm length, the maximum number of the SBP is 13, which means that the drag reduction rate and the corresponding maximum marine antifouling rate are as high as 27% and 80%, respectively.

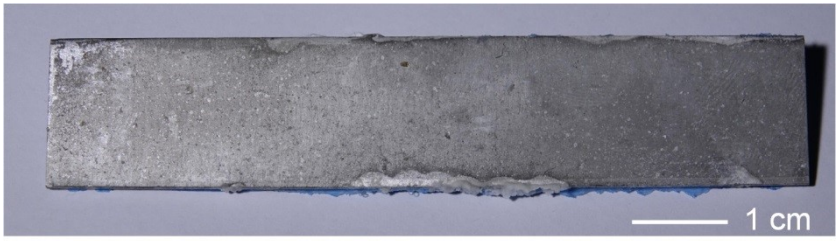

Figure S17. Image of the common Al surface immersed in simulated marine environment after 4 days. The whole Al surface was corroded.

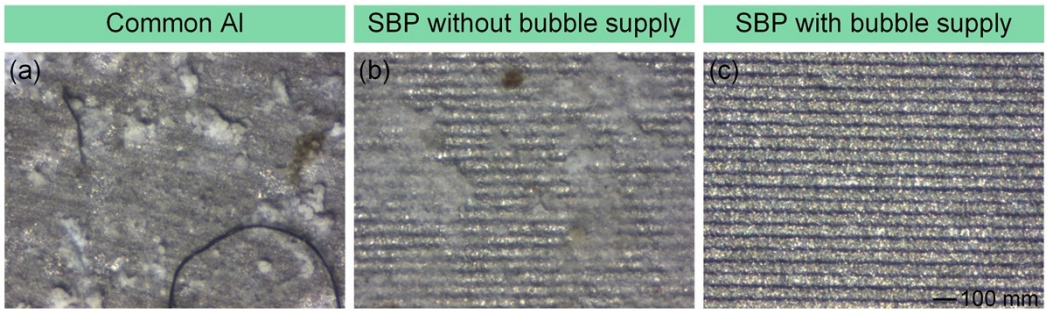

Figure S18. Images of the common Al surface, SBP without bubble supply, and SBP with bubble supply immersed in simulated marine environment after 4 days. The common Al surface was covered with a thick layer of contaminant. The surface of the SBP without bubble supply also covered a layer of contaminant, which meant that the micro-groove structure on the SBP was covered by the contaminant. However, the surface of SBP with bubble supply remained clean.

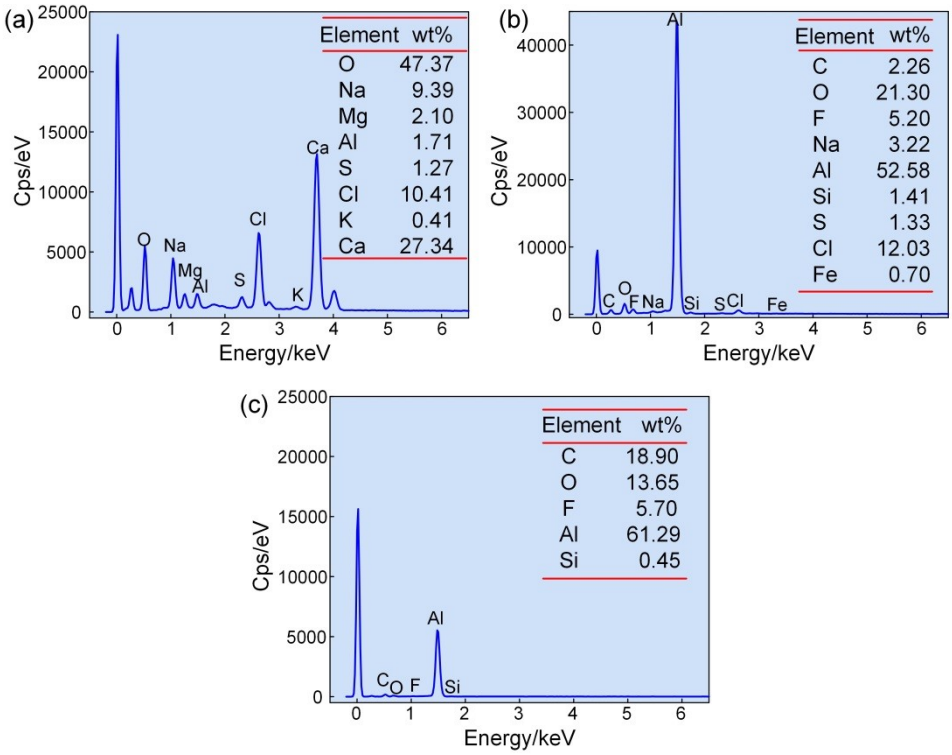

Figure S19. Chemical analysis of different surfaces. (a) EDS of the common Al surface. (b) EDS of the SBP without bubble supply. (c) EDS of the SBP with bubble suppyly. According to Figure S16(a), it can be seen that the appearance of Na, Mg, S,Cl, K, and Ca element on the common Al surface and the decreasing of the Al element, which are due to the severe surface corrosion by the seawater and the fouling by the marine organisms. Although the SBP has a antifouling capability, it is still fouled by the marine organisms in the marine environment due to the lack of air layer replenishment, as shown in Figure S16(b). However, on the SBP surface with bubble supply, the surface elements are almost unchanged from before the experiment, which is because the spontaneous fast moving air film could prevent the attachment of the primary colonizers and achieve the antifouling.

Tables

Table S1. Factor code of the Box-Behnken design optimization

Code	Rotating circle radius r /mm	Start rotation angle θ_1 /°	End rotation angle θ_2 /°
+1	28	163	186
0	22	160	180
-1	16	157	174

Table S2. Experimental results of the Box-Behnken design optimization

Sample	Factor and level combination			Response: average transportation velocity v_a/mm·s^{-1}
	r /mm	θ_1 /°	θ_2 /°	
1	22	157	174	242
2	22	163	174	200
3	22	157	186	224
4	22	163	186	318
5	16	157	180	200
6	16	163	180	265
7	28	157	180	297
8	28	163	180	248
9	16	160	174	182
10	16	160	186	343
11	28	160	174	326
12	28	160	186	262
13	22	160	180	420
14	22	160	180	400
15	22	160	180	410

Table S3. The variance analysis of the experimental results

Source of variance	Sum of squares	Degree of freedom	Mean squares	*F* value	*P* value
Model	85624.48	9	9513.83	119.15	< 0.0001
r	2556.13	1	2556.13	32.01	0.0024
θ_1	578.00	1	578.00	7.24	0.0433
θ_2	4851.12	1	4851.12	60.75	0.0006
$r\cdot\theta_1$	3249.00	1	3249.00	40.69	0.0014
$r\cdot\theta_2$	12656.25	1	12656.25	158.50	< 0.0001
$\theta_1\cdot\theta_2$	4624.00	1	4624.00	57.91	0.0006
r^2	14480.83	1	14480.83	181.35	< 0.0001
θ_1^2	33235.44	1	33235.44	416.22	< 0.0001
θ_2^2	17642.83	1	17642.83	220.95	< 0.0001
Residual error	399.25	5	79.85	—	—
Lack of fit	199.25	3	66.42	0.6642	0.6474
Error	200.00	2	100.00	—	—
Total	86023.73	14	—	—	—

Note：$P \le 0.01$ means highly significant; $0.01 \le P \le 0.05$ means significant; $P \ge 0.05$ means insignificant.

Based on the aforementioned results, we can obtained a fitted equation for the influence of the r, θ_1, and θ_2 on the average transportation velocity v_a, as follows,

$$\begin{aligned} v = &-291129.58 + 3071.00\theta_1 + 427.50\theta_2 + 614.10r + \\ &1.88\theta_1\theta_2 - 1.58\theta_1 r - 1.56\theta_2 r - 10.54\theta_1^2 - 1.92\theta_2^2\theta_2^2 - 1.74r^2 \end{aligned} \tag{S3}$$

It can be seen from the *P* value of Table S3 that the main influence order on v_a was $\theta_2 > r > \theta_1$. Moreover, r and θ_1, r and θ_1, and θ_1 and θ_2 had the interactive influence on v_a, which meant that the variation law of one factor on v_a might vary with the variation of the other one, as shown in Figure S7. We then determined that the constraint condition on the optimization model was

$$\begin{cases} v_{a\text{-}o} = \max v_a \\ r \in [16,28] \\ \theta_1 \in [157,163] \\ \theta_2 \in [174,186] \end{cases} \tag{S4}$$

where $v_{a\text{-}o}$ is the theoretical average transportation velocity. The optimal parameters of the SBP with r of 22.1 mm, θ_1 of 160.4°, and θ_2 of 180 were achieved and $v_{a\text{-}o}$ was 412 mm/s by the calculation from the Design-Expert software. We then fabricated an SBP with aforementioned parameters and found that the v_a was 415 mm/s, which was consistent with the calculated

theoretical value.

Table S4. Comparison of air bubble transportation velocity with reported in the literatures

Air bubble transportation method	References	Average transportation velocity v_a/mm·s^{-1}
Serial cycloid-shaped pattern	This work	444
3D structure	[1]	1
	[2]	7.25
	[3]	91
Slippery groove	[4]	7
	[5]	11
	[6]	22.3
	[7]	45
	[8]	95
Rectangular pattern	[9]	83.3
	[10]	98
	[11]	252
Wedge-shaped pattern	[12]	2
	[13]	310
	[14]	370
	[15]	317

Movies

Video S1. The transportation processes of the air bubble on the SBP, where the air bubble volume is 40 μL.

Video S2. The influence of the SBP parameters on the transportation process, where the air bubble volume is 40 μL.

Video S3. The transportation processes of the bubble on the SBP after the Box-Behnken design optimization, where the air bubble volume is 40 μL.

Video S4. The transportation processes of the bubble on the SBP with the junction optimization, where the air bubble volume is 40 μL.

Video S5. The transportation processes of the bubble on the SBP with the S-shaped track, where the air bubble volume is 40 μL.

Video S6. The underwater drag reduction behavior of the common Al with bubble supply, sample of 9 RP with bubble supply, and sample of 9 SBP with bubble supply, where the water flow rate was 0.5 $m \cdot s^{-1}$ and the air bubble flux was and 0.4 $L \cdot min^{-1}$.

Reference

1. Y. Wang, L. Zhang, W. Du, X. Zhou, Y. Guo, S. Zhao, D. Zhang, H. Chen, *Adv. Funct. Mater.*, 2023, **33**, 85-89.
2. X. Xue, C. Yu, J. Wang and L. Jiang, *ACS Nano*, 2016, **10**, 10887-10893.
3. X. Gao, F. Zhang, Z. Zhang, Z. Wang, Y. Song, G. Cheng and J. Ding, *ACS Appl. Mater. & Interfaces*, 2023, **15**, 54119-54128.
4. C. Yu, M. Cao, Z. Dong, K. Li, C. Yu, J. Wang and L. Jiang, *Adv. Funct. Mater.*, 2016, **26**, 6830-6835.
5. X. Wang, H. Bai, J. Yang, Z. Li, Y. Wu, C. Yu, L. Jiang and M. Cao, *Small*, 2021, **17** 2007803.
6. X. Wang, H. Bai, Z. Li, Y. Tian, T. Zhao and M. Cao, *Mater. Horiz.*, 2023, **10** 3351-3359.
7. C. Yu, X. Zhu, K. Li, M. Cao and L. Jiang, *Adv. Funct. Mater.*, 2017, **27** 1701605.
8. K. Zhuang, X. Yang, W. Huang, Q. Dai and X. Wang, *ACS Appl. Mater. & Interfaces*, 2021, **13**, 61780-61788.
9. Z. Wang, J. Xiong, Y. Liao, M. Xie, D. Yang, C. Zhang, Y. Chen and Z. Zou, *Chem. Eng. J.*, 2023, **474** 145352.
10. J. Yong, Q. Yang, J. Huo, X. Hou and F. Chen, *International Journal of Extreme Manufacturing*, 2022, **4** 15002.
11. D. Xie, Y. Sun, Y. Wu, K. Wang, G. Wang, F. Zang and G. Ding, *Adv. Mater.*, 2023, **35** e2208645.
12. X. Xiao, S. Li, X. Zhu, C. Zhang, F. Jiang, C. Yu and L. Jiang, *Nano Lett.*, 2021, **21**, 2117-2123.
13. Z. Liu, H. Zhang, Y. Han, L. Huang, Y. Chen, J. Liu, X. Wang, X. Liu and S. Ling, *ACS Appl. Mater. & Interfaces*, 2019, **11**, 23808-23814.
14. H. Ma, M. Cao, C. Zhang, Z. Bei, K. Li, C. Yu and L. Jiang, *Adv. Funct. Mater.*, 2018, **28** 1705091.
15. J. Song, Z. Liu, X. Wang, H. Liu, Y. Lu, X. Deng, C. J. Carmalt and I. P. Parkin, *J. Mater. Chem. A*, 2019, **7**, 13567-13576.